# Prediction of coherent vortices in an impinging jet with unsteady averaging and a simple turbulent model

G. Le Song *, M. Prud'homme

*Department of Mechanical Engineering, École Polytechnique de Montréal, C.P. 6079, Succ. Centre-ville, Montréal, Québec, Canada H3C 3A7*

## Abstract

The classical problem of a plane jet impinging on a flat surface is used here as a test to show that it is possible to use URANS and steady boundary conditions to predict coherent structures in the flow field from a simple model with the unsteady time and ensemble averaging of the quantities proposed by Ha Minh. The two-equation model of Myong and Kasagi, where the damping functions have the appropriate asymptotic behaviour near the wall, is used to solve the problem in two dimensions, for a jet located at a distance equal to ten times the nozzle width, using control volumes and second order finite-differences in time and space. It is found that the unsteady averaging approach of Ha Minh is able to reproduce the coherent vortices observed experimentally in the jet. Spectral analysis shows that the coherent part of the numerical solution is compatible with the vorticity dynamics near the nozzle. Overall, computational results show that the presence of coherent mean field components in the solution, if they are predicted, will improve the performance of even a simple eddy-viscosity model.
© 2007 Elsevier Inc. All rights reserved.

*Keywords:* Unsteady time-averaging; Turbulence

## 1. Introduction

The flow of an impinging jet on a surface remains a classical problem in turbulence. It is one of the typical situations where heat and fluid flow are tightly linked together. It involves at the same time instabilities; streamline curvature effects, a free shear flow region and a wall flow region. Another typical feature of jets is the presence of coherent structures downstream of the nozzle where the intensity of the turbulence increases to reach a maximum. Tsubokura et al. (1997, 2003) for instance predicted these structures by large eddy simulation (LES) for a plane jet at $Re = 6000$. They had to introduce however a small amplitude time and space disturbance into the velocity profile at the nozzle in order to generate the coherent vortices

and three-dimensional effects. Alternatively, we wish to show in this paper that it is possible to obtain coherent vortices in the jet from completely steady boundary conditions using unsteady Reynolds averaged Navier–Stokes equations (URANS) along with the unsteady averaging approach put forward by Ha Minh (1994), Ha Minh and Kourta (1993).

The central idea in Ha Minh's approach is the presence of a deterministic coherent part in a turbulent quantity. Let us recall that the ensemble average of a given variable $F$ at some position $\mathbf{x}$ and time t is defined as:

$$\overline{F}(\mathbf{x}, t) = \lim_{N \to \infty} \frac{1}{N} \sum_{n=1}^{N} F(\mathbf{x}, t)_n \tag{1}$$

where $F_n$ is the value that one would obtain if the experiment was to be repeated from the beginning for the $n$th time. Formally, the time average $\overline{\overline{F}}$ of the variable may be obtained by integration of the local value of $\overline{F}$ as follows:

---

* Corresponding author. Address: Polytechnic Institute of Ho Chi Minh City, 268 Ly Thuong Kiet, 10th district, Ho Chi Minh City, Vietnam.

*E-mail addresses:* lsgiang@hcmut.edu.vn (G. Le Song), miprud@meca.polymtl.ca (M. Prud'homme).

$$\overline{\overline{F}}(\mathbf{x}) = \underbrace{\lim_{T \to \infty}}\frac{1}{T}\int_0^T \overline{F}(\mathbf{x}, t)\,\mathrm{d}t \qquad (2)$$

The coherent part $\widetilde{F}$ of the variable, unsteady but not random, is simply defined as the difference $\widetilde{F} = \overline{F} - \overline{\overline{F}}$ of the averages. This decomposition is essentially introduced to determine the time-averaged Reynolds stresses from the URANS solutions, as we will see later on. In steady flows, the coherent part vanishes. In transient, periodic or pseudo-periodic flows, the coherent part no longer vanishes, but its (time) mean value remains equal to zero. We shall not make any particular assumptions here regarding periodicity. It will be seen also that this decomposition can be used to improve-to some extent-the performance of eddy-viscosity turbulence models. We purposely select a low Reynolds number version of the $k$–$\varepsilon$ model to illustrate the point. The damping functions designed for boundary layer flows are adjusted however to the context of a vanishing shear stress near the stagnation point.

The impinging jet problem, apart from its complexity from the point of view of fluid mechanics, also has a very practical interest as an efficient mean to heat, cool or dry materials, since strong heat and mass transfer rates occur near the stagnation points. So far, both plane and round jets have been studied experimentally. Valuable contributions were made in the case of a plane jet by Tsubokura et al. (1997) and Sakakibara et al. (1978) among others. It is found that azimuthal vortices are generated downstream of the nozzle in round jets, while two-dimensional vortices with the axis oriented spanwise occur in plane jets. These eddies originate from a Kelvin–Helmholtz instability of the flow in the potential core region of the jet located near the nozzle. The plane jet, in contrast to the round jet, has no clear single unstable mode associated with a particular Strouhal number. In fact, many different modes can be indistinctly excited downstream of the nozzle as reported by Gutmark and Ho (1983). The energy of the primary instability at some frequency grows as it is carried with the flow until the first sub-harmonic at one-half of the frequency starts to develop, as explained by Ho (1982). Secondary instabilities may occur also. The onset of the sub-harmonic components is closely related to the coalescence of the initial eddies. The spectral analysis of the velocity field performed by Hsiao and Huang (1990) and by Aydore and Dissimile (1997) for a free jet and by Anderson and Longmire (1995) for an impinging jet revealed that the spatial evolution of the spectrum of the transverse velocity component is directly linked to the merging of the eddies.

The coherent vortices in a plane jet are unstable spanwise, just as the round jet vortices are in the azimuthal direction, and eventually become three-dimensional structures as the disturbance grows. The most unstable mode has a wavelength equivalent to roughly two-thirds of the distance between the eddy centres, as shown analytically by Pierrehumbert and Widnall (1982) and verified by Tsubokura et al. (2003) in an impinging jet at $Re = 2000$ by

direct numerical simulation. Their computations revealed that the spanwise instability also determines the number of streamwise vortex pairs, generated by stretching, which appear downstream between the initial eddies. These streamwise vortices evolve, at lower Reynolds numbers, into coherent, organized vortices along the transverse direction in the stagnation region. These structures become increasingly distorted and indefinite as the Reynolds number increases however.

## 2. Mathematical formulation

Incompressible, constant property turbulent flow is assumed throughout the analysis. The mean velocity components $\overline{U}_i$ then satisfy the continuity equation $\partial \overline{U}_i/\partial x_i = 0$ as well as the ensemble-averaged Navier–Stokes equations:

$$\frac{\mathrm{D}\overline{U}_i}{\mathrm{D}t} = -\frac{1}{\rho}\frac{\partial \overline{P}}{\partial x_i} + \frac{\partial}{\partial x_j}\left(v\frac{\partial \overline{U}_i}{\partial x_j} - \overline{u_i u_j}\right) \qquad (3)$$

The geometry of the problem is summarized in Fig. 1. It is the same as in Tsubokura et al.'s (1997) experimental setup for a Reynolds number $Re = V_0 B/v = 6000$. The problem is solved here in two dimensions, which should be enough to capture the essential features of the turbulent flow in the $x$–$y$ plane, since the mean velocity component and the stretching effect in the spanwise direction were negligible in the plane of measurements. The boundary conditions for the present computations are also indicated.

The energy dissipation rate on the wall is evaluated from the turbulent kinetic energy as $\varepsilon_w = v(\partial k^{1/2}/\partial y)^2$. We use the empirical formula of Tsubokura et al. $\overline{V} = V_0[1 - (2x/B)^{10}]$ for the velocity profile at the nozzle. Assuming homogeneous Neumann conditions for all variables outside the jet at the top boundary works fine if the jet is laminar, but generates back flows and unrealistic high levels of $k$ inside the domain when the jet is turbulent. Instead, a small velocity $V = 0.01V_0$ can be imposed as in Fig. 1 to account for fluid entrainment. The actual value being used does not appear very consequential a posteriori for the prediction of turbulence, as long as it remains small. Tsubokura et al. for instance assumed a value equal to $0.05V_0$ for their large eddy simulation and achieved good results. For turbulent quantities, we will use $\sqrt{2k} = 0.03V$
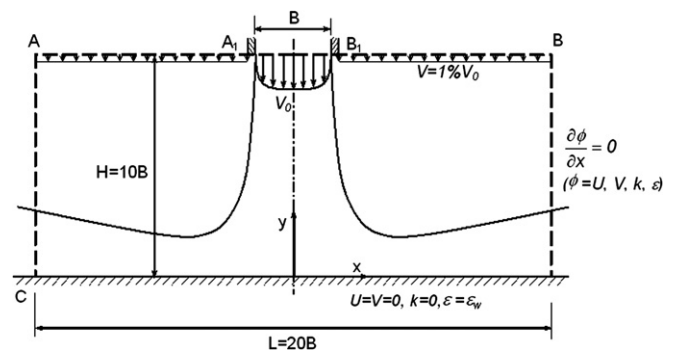


Fig. 1. Geometry and boundary conditions.

to fit Tsubokura's data inside the jet, and also outside where the value of $k$ is then very small. The dissipation rate $\varepsilon$ is set in such a way that the turbulent Reynolds number $R_T = k^2/v\varepsilon$ always remains equal to $10^5$ locally. Similar boundary conditions were also used by Craft (1991) with success. It is well known that using homogeneous Neumann conditions at the outflow boundaries is likely to cause problems for the outgoing vortices. But in the present case, the computational domain is large and the mesh sufficiently fine to keep the undesirable effects under control and confined to the vicinity of the boundary.

Closure of the momentum equations is achieved with a turbulent viscosity $v_T$ through the standard Boussinesq representation for the Reynolds stress tensor:

$$\overline{u_i u_j} = \frac{2}{3} k \delta_{ij} - v_T \left( \frac{\partial \overline{U}_i}{\partial x_j} + \frac{\partial \overline{U}_j}{\partial x_i} \right) \tag{4}$$

The turbulent viscosity is defined within the framework of a low $R_T$ version of the $k$–$\varepsilon$ model as $v_T = C_\mu f_\mu k^2/\varepsilon$, where $f_\mu$ is an appropriate damping function and $C_\mu$ a constant equal to 0.09. Using continuity, the governing equation for the mean velocity can be expressed in conservative form as:

$$\frac{\partial \overline{U}_i}{\partial t} + \frac{\partial}{\partial x_j}(\overline{U}_j \overline{U}_i) = -\frac{\partial P_{eff}}{\partial x_i} + \frac{\partial}{\partial x_j}\left( v_{eff} \frac{\partial \overline{U}_i}{\partial x_j} \right) + \frac{\partial}{\partial x_j}\left( v_{eff} \frac{\partial \overline{U}_j}{\partial x_i} \right) \tag{5}$$

In the above, $v_{eff} = v + v_T$ is the effective viscosity, while $P_{eff} = \overline{P}/\rho + 2k/3$ stands for the effective pressure. Taking the divergence of Eq. (5) yields a Poisson equation for the effective pressure field $P_{eff}$, namely:

$$\nabla^2 P_{eff} = \nabla \cdot \left( -\frac{\partial \overline{U}}{\partial t} + \mathbf{J} \right) = -\frac{\partial}{\partial t}(\nabla \cdot \overline{U}) + \nabla \cdot \mathbf{J} \tag{6}$$

The divergence of the velocity field will not be set equal to zero for the moment. The components of the $\mathbf{J}$ vector above are given by:

$$J_x = -\frac{\partial}{\partial x_j}(\overline{U U_j}) + \frac{\partial}{\partial x_j}\left\{ v_{eff} \left( \frac{\partial \overline{U}}{\partial x_j} + \frac{\partial \overline{U}_j}{\partial x} \right) \right\}$$
$$J_y = -\frac{\partial}{\partial x_j}(\overline{V U_j}) + \frac{\partial}{\partial x_j}\left\{ v_{eff} \left( \frac{\partial \overline{V}}{\partial x_j} + \frac{\partial \overline{U}_j}{\partial y} \right) \right\} \tag{7}$$

Let $\mathbf{n}$ denote the outward unit normal to the solution domain. The Poisson equation (6) for the effective pressure is solved after imposition of the Neumann condition:

$$\frac{\partial P_{eff}}{\partial n} = \left( -\frac{\partial \overline{U}}{\partial t} + \mathbf{J} \right) \cdot \mathbf{n} \tag{8}$$

everywhere over the boundary of the domain, following Gresho and Sani (1987) who showed that Eq. (8) is a better suited condition to ensure continuity on the boundary. The turbulence model used here is basically that of Myong and Kasagi (1990), with slight modifications to the damping functions, in order to extend its validity to complex flows.

Let us now examine the model in detail. The transport equations for the turbulence kinetic energy k and its dissipation rate $\varepsilon$ are represented by:

$$\frac{Dk}{Dt} = \frac{\partial}{\partial x_i}\left( v_k \frac{\partial k}{\partial x_i} \right) + \mathscr{P} - \varepsilon$$
$$\frac{D\varepsilon}{Dt} = \frac{\partial}{\partial x_i}\left( v_\varepsilon \frac{\partial \varepsilon}{\partial x_i} \right) + C_{1\varepsilon} \frac{\varepsilon \mathscr{P}}{k} - C_{2\varepsilon} f_{2\varepsilon} \frac{\varepsilon^2}{k} \tag{9}$$

The model constants are $C_{1\varepsilon} = 1.4$, $C_{2\varepsilon} = 1.8$, with $\sigma_k = 1.4$, $\sigma_\varepsilon = 1.3$ in $v_k = v + v_T/\sigma_k$ and $v_\varepsilon = v + v_T/\sigma_\varepsilon$. Using continuity and the Boussinesq closure equation (4), the turbulent energy generation rate $\mathscr{P}$ becomes:

$$\mathscr{P} = -\overline{u_i u_j} \frac{\partial \overline{U}_i}{\partial x_j} = v_T \frac{\partial \overline{U}_i}{\partial x_j}\left( \frac{\partial \overline{U}_i}{\partial x_j} + \frac{\partial \overline{U}_j}{\partial x_i} \right) \tag{10}$$

The original damping functions $f_\mu$ and $f_{2\varepsilon}$ in the Myong and Kasagi model may be expressed in terms of the turbulent Reynolds number $R_T$ and the normalised distance from the wall $y^+ = u_* y/v$ as follows:

$$f_\mu = \left( 1 + \frac{3.45}{R_T^{1/2}} \right)(1 - e^{-y^+/70})$$
$$f_{2\varepsilon} = \left( 1 - \frac{2}{9} e^{-R_T^2/36} \right)(1 - e^{-y^+/5})^2 \tag{11}$$

The first factor involving $R_T$ in the damping function $f_\mu$ is based on an evaluation of the mixing length. The second factor is introduced to constrain $f_\mu$ to behave as $1/y^+$ as $y^+$ approaches zero as reported in the analysis of Patel et al. (1985), so that the $C_\mu f_\mu k^2/\varepsilon$ profile remains cubic in the near-wall region of boundary layers and pipe or channel flows as well. Within the range $0 < y^+ < 5$ approximately, the mean velocity profile is linear. Expansion shows that $\varepsilon = \varepsilon_w + \mathcal{O}(y^+)$ in this region, while k and the turbulent shear stress behave as $y^{+2}$ and $y^{+3}$, respectively. It follows that $v_T$ must be locally proportional to $y^{+3}$ also.

In the same way, the first factor in the damping function $f_{2\varepsilon}$ originates from the model of Hanjalić and Launder (1976). It is intended to match the experimental data for k during the final period of decay of turbulence behind a grid. The purpose of the second factor is to ensure the quadratic form of the $f_{2\varepsilon}$ profile near the wall, where $\varepsilon^2/k$ is proportional to $1/y^{+2}$. A closer examination of Eq. (9) reveals that the diffusion term, which has a finite value at the wall, must be balanced by $f_{2\varepsilon}\varepsilon^2/k$ since all the remaining terms in the equation vanish. For larger values of $y^+$, the model is consistent with the laws of the wall for k and $\varepsilon$ within the logarithmic zone in channel/boundary layer flows, with a predicted value of 0.395 for the von Kármán constant $\kappa$. Details are provided in Appendix.

As mentioned earlier, the impinging jet flow is complex, involving regions of low turbulent Reynolds number far from the wall where y is large, and also near the stagnation point where the friction velocity $u_*$ is nearly zero. An attempt is made here to extend the validity of the damping

functions to these regions as well, by setting aside any reference to $y$ in the damping functions. We use instead:

$$y_m = a_0 R_T^{1/2} + a_1 R_T + a_2 R_T^2 + a_3 R_T^3 + a_4 R_T^4 \qquad (12)$$

in the second factors of the slightly modified damping functions:

$$f_\mu = \left(1 + \frac{3.45}{R_T^{1/2}}\right)(1 - e^{-y_m/A_1})$$

$$f_{2\varepsilon} = \left(1 - \frac{2}{9}e^{-R_T^2/36}\right)(1 - e^{-y_m/A_2})^2 \qquad (13)$$

To make sure that the model performs as well as before in simple flows with the new damping functions, the coefficient values $a_0$, $a_1$ and so forth displayed in Table 1 are optimised to reproduce as closely as possible the direct numerical simulations of Mansour et al. (1988) for plane channel flow.

Computations reveal that the new variable $y_m$ in Eq. (12) behaves asymptotically as $y^+$ near the wall, that is, within the mixed region and the viscous sublayer.

To see how the time-averaged Reynolds stresses may be obtained from the ensemble-averaged quantities $\overline{U}$, $\overline{V}$, $k$ and $\varepsilon$, one can split the instantaneous value of a variable $F$ at some position $\mathbf{x}$ and time $t$ as:

$$F(\mathbf{x}, t) = \overline{\overline{F}}(\mathbf{x}) + \widetilde{F}(\mathbf{x}, t) + f(\mathbf{x}, t) \qquad (14)$$

where $\overline{\overline{F}}$ and $\widetilde{F}$ are defined from Eqs. (1) and (2) respectively, and $f$ is the random turbulent motion. The ensemble average procedure extracts organized motion from the fluctuating field data. The components of $F$ share the same interesting properties as those of the phase averaging decomposition used by Hussain and Reynolds (1970) and Reynolds and Hussain (1972) to study organised wave motion in turbulent shear flow. In particular, it follows from the definitions that the coherent and fluctuating parts of $F$ are uncorrelated and the time average of their product vanishes. The time average of Eq. (3) yields an equation for the mean field quantities which is identical, except for the Reynolds stresses which are now replaced by the sum of two terms, as detailed in Reynolds and Hussain (1972) for instance. For two arbitrary velocities $F$ and $G$ we have:

$$\overline{fg} \rightarrow \overline{\overline{\widetilde{F}\,\widetilde{G}}} + \overline{\overline{fg}} \qquad (15)$$

The product of the coherent parts in Eq. (15) can be computed directly. The other term involving the fluctuations is evaluated from the time-averaged solution of the velocity field with the help of the Boussinesq closure Eq. (4). The short-hand notation $\overline{f'g'}$ will be used later on for the sum of the two terms.

## 3. Numerical procedure

The problem is solved in dimensionless form over a uniform mesh, after scaling lengths, velocities and pressure with respect to the nozzle width $B$, maximum inlet jet velocity $V_0$ and $\rho V_0^2$ respectively. Discretization is performed by finite differences, within the control volume approach. The transport equation for a given variable $\phi$ may be recast in the form:

$$\frac{\partial \phi}{\partial t} + \frac{\partial}{\partial x_j}(\overline{U}_j \phi) = \frac{\partial}{\partial x_j}\left(\Gamma_\phi \frac{\partial \phi}{\partial x_j}\right) + S(\phi) \qquad (16)$$

where $\Gamma_\phi$ is a diffusion coefficient and $S(\phi)$ a source term. Table 2 shows how the latter are defined for the mean velocity components $\overline{U}$, $\overline{V}$ and the turbulent variables $k$ and $\varepsilon$.

The time discretization of Eq. (16) is performed using the implicit Crank–Nicholson scheme for the diffusive terms and the explicit Adams–Bashforth scheme for the convective terms in order to uncouple the transport equations. Both schemes are second-order accurate. They can be used simultaneously without causing stability problems since very small time steps are used in the calculations. The Adams–Bashforth scheme is used also for the variables involved in the source terms, apart from pressure, which is evaluated before the other variables at every time step. Pressure is evaluated in fact at time $t^{n+1/2}$ from the known field values at time $t^n$. The other variables are determined at time $t^{n+1}$ in two steps, according to the ADI method as follows:

$$\frac{\Delta \phi^{n+1/2}}{\Delta t/2} - \frac{\partial}{\partial x}\left(\Gamma_\phi \frac{\partial \Delta \phi^{n+1/2}}{\partial x}\right)$$

$$= \frac{\partial}{\partial x_j}\left(-\overline{U}_j^* \phi_i^* + \Gamma_\phi \frac{\partial \phi^n}{\partial x_j}\right) + S(\phi^*)$$

$$\frac{\Delta \phi^n}{\Delta t/2} - \frac{\partial}{\partial y}\left(\Gamma_\phi \frac{\partial \Delta \phi^n}{\partial y}\right) \qquad (17)$$

$$= \frac{\partial}{\partial x_j}\left(-\overline{U}_j^* \phi_i^* + \Gamma_\phi \frac{\partial \phi^{n+1/2}}{\partial x_j}\right) + S(\phi^*)$$

In the above, $\Delta \phi^{n+1/2} = \phi^{n+1/2} - \phi^n$ and $\Delta \phi^n = \phi^n - \phi^{n+1/2}$, while $\phi^* = 3\phi^n/2 - \phi^{n-1}/2$. Both equations are integrated over a control volume. The divergence theorem is used to transform each equation into a sum of flux integrals over the control surfaces. Spatial discretization of the gradient fluxes is achieved according to central difference schemes.

Table 1
Parameter values in Eqs. (11) and (12)

| $a_0$ | $a_1$ | $a_2$ | $a_3$ | $a_4$ | $A_1$ | $A_2$ |
|---|---|---|---|---|---|---|
| 3.60 | 5.00E−3 | 3.00E−6 | −2.50E−6 | 4.00E−8 | 80 | 4 |

Table 2
Diffusion coefficients and source terms in Eq. (16) for $\overline{U}$, $\overline{V}$, $k$ and $\varepsilon$

| $\phi$ | $\Gamma_\phi$ | $S$ |
|---|---|---|
| $\overline{U}$ | $\nu_{\text{eff}}$ | $-\frac{\partial P_{\text{eff}}}{\partial x} + \frac{\partial}{\partial x_j}\left(\nu_{\text{eff}} \frac{\partial \overline{U}_j}{\partial x}\right)$ |
| $\overline{V}$ | $\nu_{\text{eff}}$ | $-\frac{\partial P_{\text{eff}}}{\partial y} + \frac{\partial}{\partial x_j}\left(\nu_{\text{eff}} \frac{\partial \overline{U}_j}{\partial y}\right)$ |
| $k$ | $\nu_k$ | $\mathscr{P} - \varepsilon$ |
| $\varepsilon$ | $\nu_\varepsilon$ | $C_{1\varepsilon} \frac{\varepsilon \mathscr{P}}{k} - C_{2\varepsilon} f_{2\varepsilon} \frac{\varepsilon^2}{k}$ |

Second, and wherever possible, fourth order interpolations are used to evaluate the convective fluxes and other derivatives in terms of the nodal values. The result is a discrete approximation of Eq. (17) at every internal node, defining a tri-diagonal system for the new field values, which is solved by standard methods. The same approach is used on the boundary surfaces where Neumann conditions are specified. The only difference between boundary and internal nodes is that the gradients on the face of the control volume adjacent to the boundary are now replaced by the values prescribed by the Neumann condition. This leads to a modified discrete equation on the boundary.

Only the Adams–Bashforth formulation is used for pressure however, with central differences for the time derivative at $t^{n+1/2}$. The divergence of the velocity field at $t^n$ is retained during the computations in order to improve stability. Using the divergence theorem once more on Eq. (6) yields in compact form:

$$\int_A \frac{\partial P_{\mathrm{eff}}}{\partial n}\,\mathrm{d}A = \int_A \left(-\frac{\overline{U}^n}{\Delta t} + J_n^*\right)\mathrm{d}A \qquad (18)$$

The flux integral on the right-hand side is split and evaluated over each control volume face in the same way as before. When the control volume face is located on a boundary, the normal derivative of the pressure is imposed by Eq. (8). If the face lies on the right boundary for instance, the local pressure derivative will be computed as follows:

$$\frac{\partial P_{\mathrm{eff}}}{\partial x} = J_x^* - \frac{2\overline{U}^n - 3\overline{U}^{n-1} + \overline{U}^{n-2}}{\Delta t} \qquad (19)$$

The flux of $J_x^*$ through the east control volume face would then cancel on both sides of Eq. (18), leaving us with a specialized form of the finite difference equation for pressure. The discrete counterpart of Eq. (18) is a linear system of the form $[\mathbf{A}]\{\mathbf{P}\} = \{\mathbf{C}\}$ where $[\mathbf{A}]$ is a singular matrix. Unstaggered grids are used in the present study however. In order to enforce solution compatibility, that is, to obtain a realistic pressure field for the velocity field solution, it is important that the sum of the elements of the source term $\{\mathbf{C}\}$ vanishes. For this purpose, the sum is redistributed evenly between all the elements of the source term following Briley (1974). The system is finally solved with the multi-grid method of Ghia et al. (1982), using the SLOR algorithm.

All the results presented below are computed using a time step $\Delta t = 7.5\text{E}{-}4$, with a uniform 641 by 321 mesh, for a total simulation time $t_f$ equal to 614.4. The time averages in Eq. (2) are evaluated from $2^{13}$ local samples, all evenly spaced in time by 200 time steps $\Delta t$. The Fourier transforms used for spectral analysis are calculated from four times as many samples, all evenly spaced by 50 time steps. A grid dependence test was performed for a half jet, that is, for $x > 0$, using a 641 by 641 mesh and a 321 by 321 mesh. Nearly identical results were obtained from both grids for the mean velocity components and the tur-

bulence variables as well, indicating that the present mesh is accurate enough for the complete jet.

## 4. Results

With the present model and steady boundary conditions of Fig. 1, the coherent structures are only predictable within the unsteady approach of Ha Minh. Otherwise, the solutions of the ensemble-averaged equations for the mean and turbulent quantities remain completely steady. It is worth mentioning also that the models of Lam and Bremhorst (1981), Launder and Sharma (1974), Craft et al. (1997) were adapted to the context of unsteady averaging, just like the model of Myong and Kasagi, and failed to reproduce the coherent vortices in the jet. Further tests in plane channel flow with the model of Myong and Kasagi showed that it also produced better results for $k$ and $\varepsilon$ than the three models above. This might be a clue on why the model of Myong and Kasagi stands out here as the only one able to predict the coherent structures.

The ensemble-averaged vorticity field shown in Fig. 2 provides a general representation of the impinging jet flow at some particular moment in time. One can first notice that the loss of symmetry of the mean vorticity field with respect to the jet axis at $x = 0$ observed experimentally is reproduced in the numerical solution. The potential core of the jet is visible near the nozzle. The shear layers on each side are independent at first. Each individual layer shows oscillations in the near and developing jet region. The instabilities grow, generating counter-rotating eddies which form a coherent structure downstream. A very similar coherent structure pattern has been observed experimentally by Angioletti et al. (2003) in a plane impinging jet at $Re = 1500$.

Further downstream, the two series merge together and flow down as a single series of eddies, increasing in size as pairing occurs. As the impinging jet spreads, turbulence intensity increases gradually to reach a maximum around 7 or 8 nozzle widths downstream. Intense stretching and redistribution occurs near the stagnation point. Along the wall, the thickness of the jet increases linearly with the distance from the stagnation point. The coherent structures in the transverse direction found in the stagnation region at
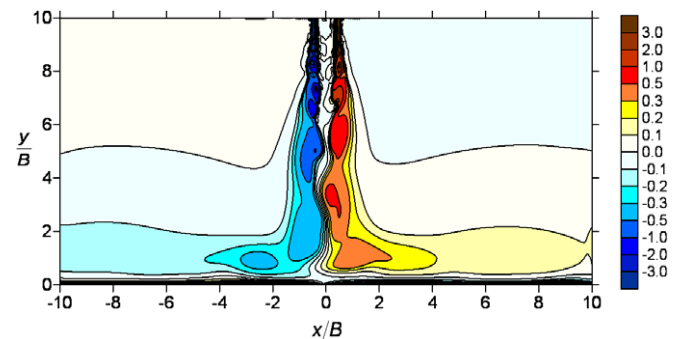


Fig. 2. Instantaneous mean vorticity field $\overline{\Omega}$.

lower Reynolds numbers are already much less distinct at $Re = 6000$ as reported by Tsubokura et al. (2003). It is interesting therefore to verify how the present two-dimensional solution is affected by the averaging effect in the spanwise direction for all variables. The time-averaged results are now investigated from the point of view of the semi-deterministic approach and compared with the available data of Tsubokura. Let us consider the impinging jet first.

Fig. 3 shows the time-averaged velocity profile $\overline{\overline{V}}$ across the jet at three locations: near the nozzle, near the wall and half-way between. Everywhere, the numerical predictions closely match the experimental data of Tsubokura et al. (1997) for the mean velocity. The level of agreement is only moderate for the predictions of the turbulent quantities, as can be seen from Figs. 4, 5, 7. The discrepancies are essentially due to the limitations of the present turbulent model which is based on the Boussinesq closure. Nevertheless, it is clear from Fig. 4 for instance that the contribution of the coherent part of the solution, which is made possible by the unsteady averaging of Ha Minh, improves the prediction of even this simple model up to a certain extent. Similar conclusions were reached by Reynolds and Hussain (1972), who found it essential to include a representation of the wave-induced oscillations in the Reynolds stresses in models attempting to reproduce organized waves in turbulent shear flow. Using linear stability analysis, they found out that significant improvements in the predictions were possible even with a very simple eddy viscosity model.
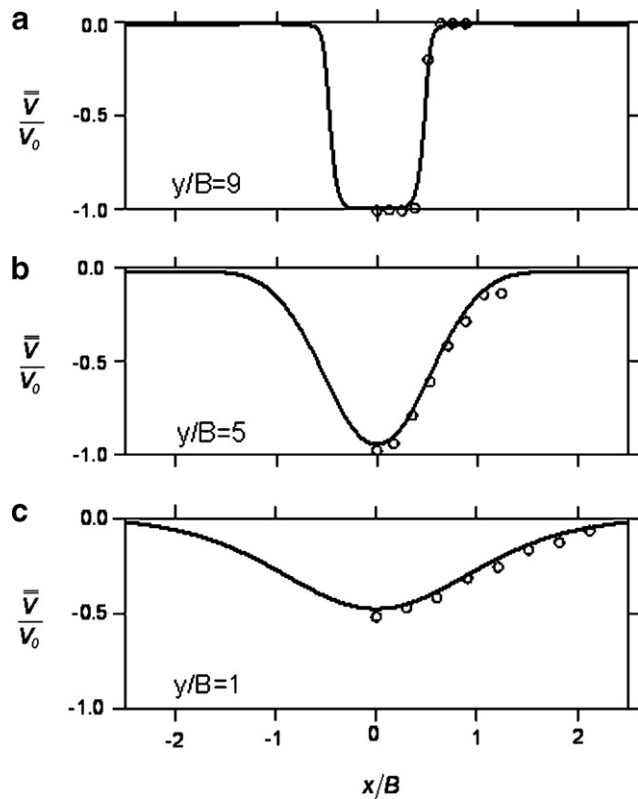
There is better agreement between Tsubokura's data and the present simulations in the simple shear layer flow near the nozzle than elsewhere, as expected. The turbulent energy component $\overline{v'v'}$ is reproduced with greater accuracy everywhere in the impinging jet than the component associated with the transverse fluctuations $u'$, which is underestimated by Eq. (4). This does not come out as a surprise, since the Boussinesq closure is known to provide a rather coarse representation of the anisotropy between the turbulent kinetic energy components. This is true in particular when the calculations based on Eq. (4) involve the secondary strain rates in the flow instead of the main strain rates.

The Boussinesq closure plainly fails at $y/B = 1$, predicting unphysical negative values for the transverse component near the axis of the jet, which were discarded from the graph. It is precisely on this plot that the improvement on the modeling predictions due to the coherent part of the flow is the most visible. The correction is also clear on the distribution of the turbulent kinetic energy components along the jet axis represented in Fig. 5. The Boussinesq closure also fails here to predict a positive value for the trans-
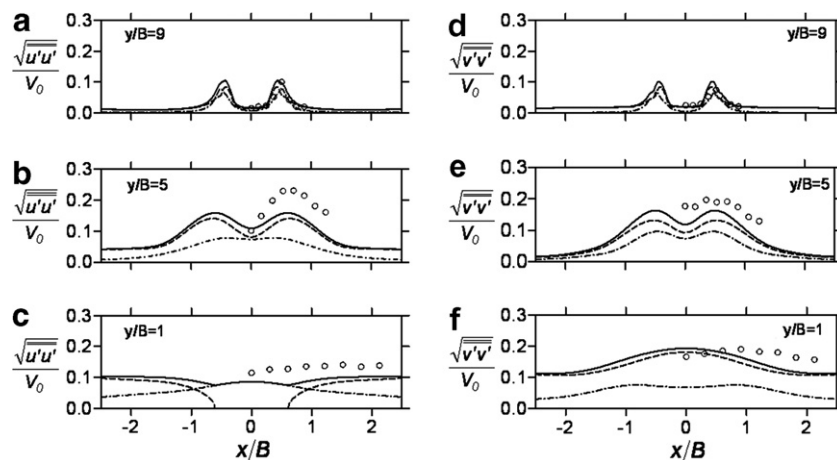


Fig. 3. Jet velocity profiles $\overline{\overline{V}}/V_0$ versus $x$ at $y/B = 1, 5, 9$.



Fig. 4. Components of turbulent kinetic energy versus $x$ at $y/B = 1, 5, 9$.
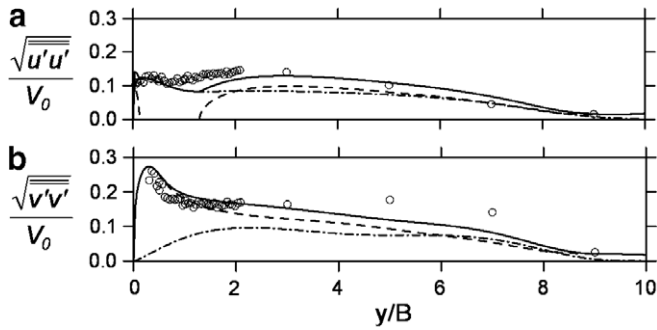
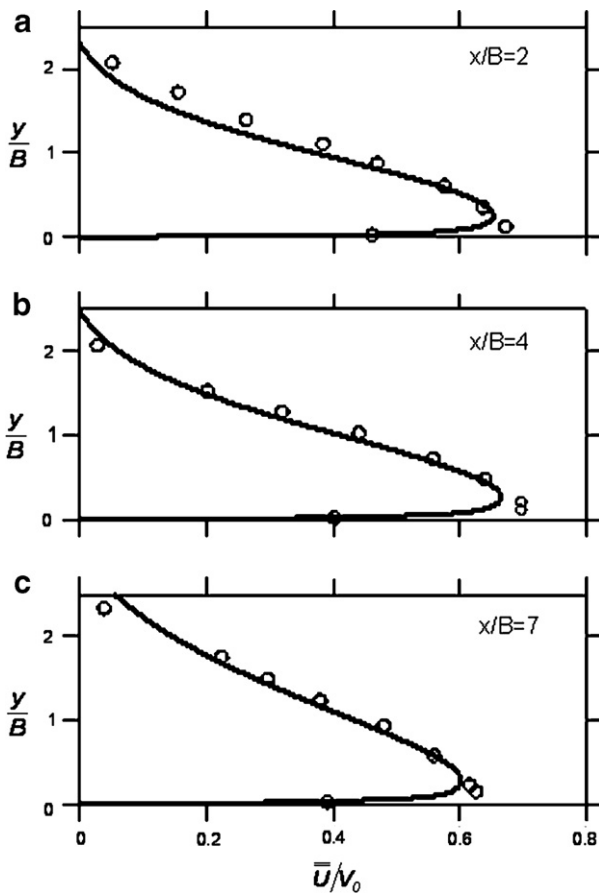Fig. 5. Turbulent kinetic energy components on the jet axis. Captions as in Fig. 4.



Fig. 6. Jet velocity profiles $\overline{U}/V_0$ versus $y$ at $x/B = 2, 4$. Captions as in Fig. 3.
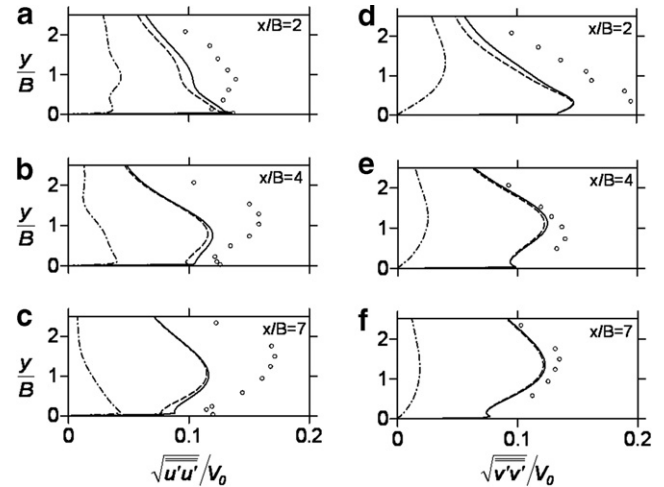


Fig. 7. Components of turbulent kinetic energy versus $y$ at $x/B = 2, 4, 7$. Captions as in Fig. 4.

appears reasonably well predicted at some distance from the stagnation point. From a physical point of view, it is well established, as explained by Bradshaw (1973) for instance, that streamline curvature as it occurs in the stagnation region where the impinging jet turns sideways and the flow is accelerating generates high levels of turbulent shear stress and kinetic energy, that turbulence models based on the Boussinesq closure are not able to reproduce adequately.

The coalescence process transforming the small eddies generated near the nozzle into the larger eddies found further downstream generates sub-harmonics of the primary and secondary instabilities. This is quite visible on Fig. 8, which is also similar to what Angioletti et al. (2003) observed in their experiment. Five eddies, labelled from V1 to V5, are selected within the coherent velocity field. The successive images show that the original eddies V1 and V2 are completely merged together at time $t = 1.8$ and that pairing is about to occur for eddies V3 and V4. A larger structure is formed as a result. Conservation of angular momentum requires that the speed of rotation of the new eddy decreases. A first sub-harmonic appears in this way, and the spectral energy of that component will grow until a new pairing occurs and the second sub-harmonic is generated. This process, taking place simultaneously on both sides of the jet, goes on along the entire potential core.

Examination of the spectral composition of the coherent velocities can be helpful at this point to confirm that this unsteady velocity field has a physical meaning and is not just merely a numerical effect. The power spectra $E_F$ of some quantity $F$ is based on the Fourier transform:

$$\Phi_F(\mathbf{r}, \omega) = \frac{1}{2\pi} \int_{-\infty}^{\infty} F(\mathbf{r}, t) \exp(-i\omega t) \, dt \qquad (20)$$

It is defined as the modulus squared of the transform divided by $2\pi$, i.e. $2\pi E_F = \|\Phi_F\|^2$. Let the Strouhal number
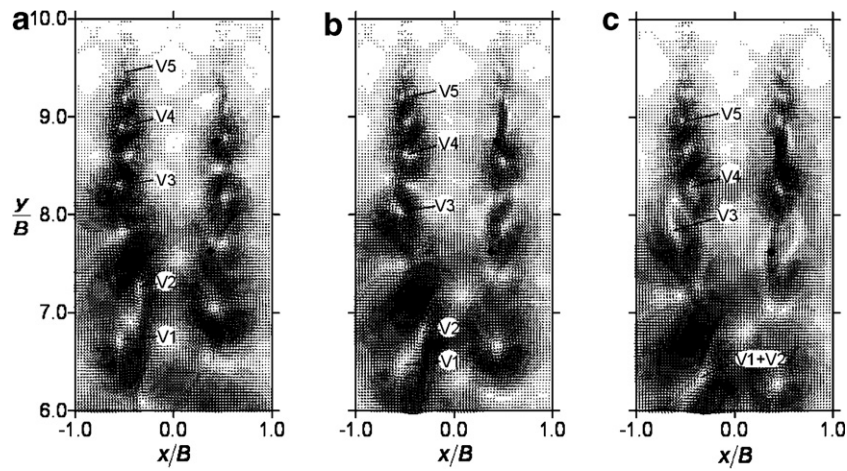
verse component in the vicinity of the plate. But the agreement between the unsteady averaged predictions for the two components and the experimental data is quite good overall.

Considering now the wall jet, one can see from Fig. 6 that the transverse velocity component $\overline{\overline{U}}$ is well predicted also except, perhaps, very close to the wall. The turbulent kinetic energy components, however, are not reproduced with better accuracy than they were in the impinging jet. As one can tell from Fig. 7, $\overline{v'v'}$ is the only component that

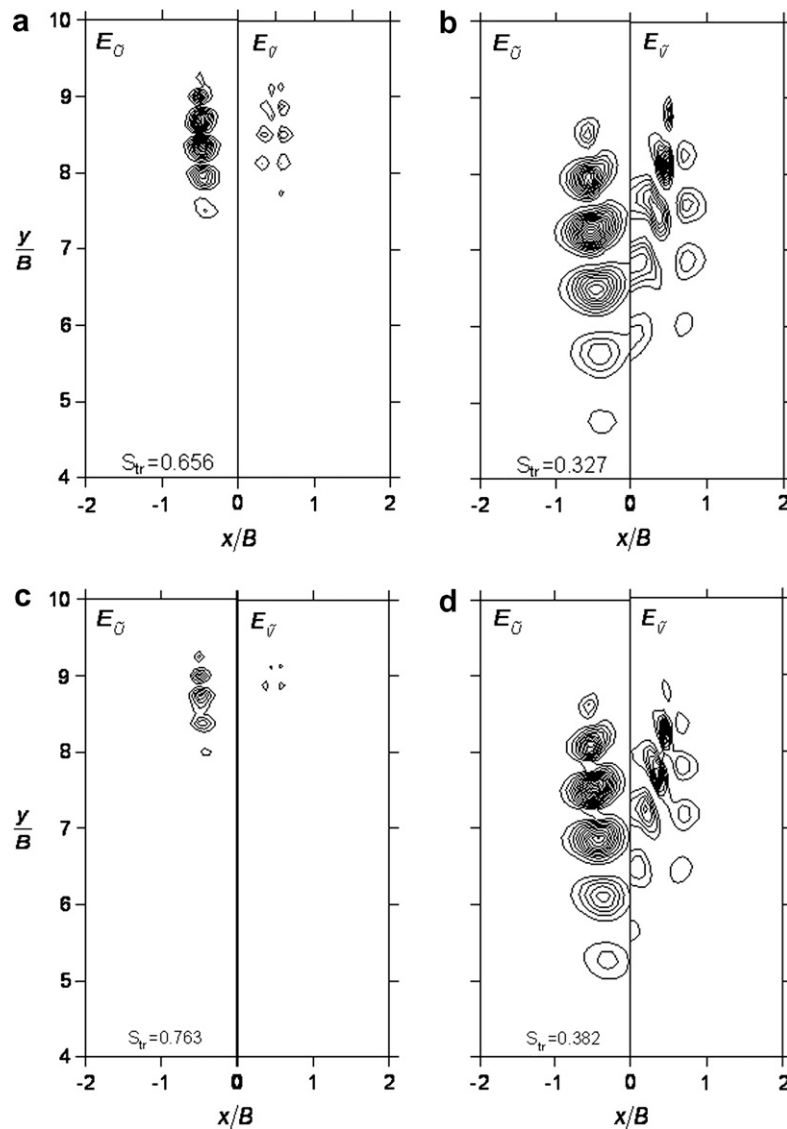Fig. 8. Evolution of the coherent velocity field $\widetilde{U}$, $\widetilde{V}$ in the impinging jet.



Fig. 9. Contour lines of power density spectra $E_U$ and $E_V$ at Strouhal numbers $S_{\mathrm{tr}} = 0.327, 0.382, 0.656, 0.763$.

$S_{\mathrm{tr}} = Bf/V_0$ represent the normalized frequency $f = \omega/2\pi$. The spectra are easily obtained as a step of the post-treatment of the solution using standard numerical packages.
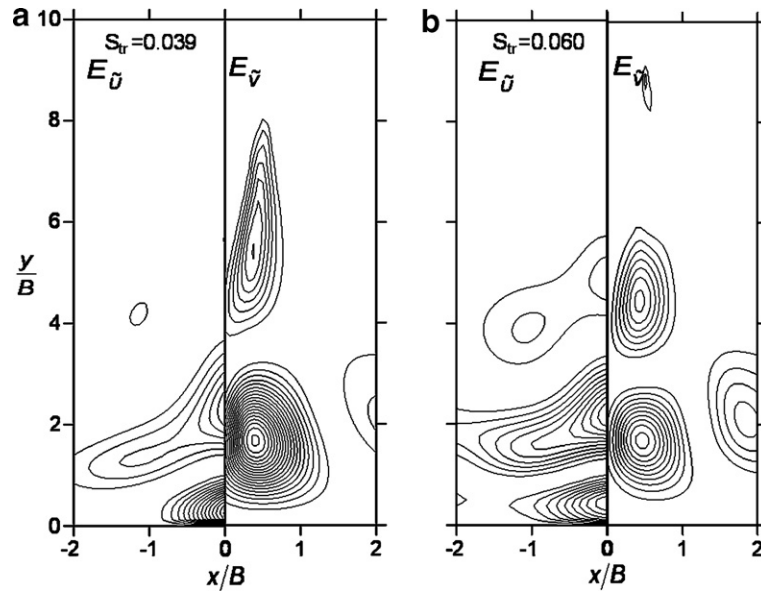
Fig. 10. Contour lines of power density spectra $E_U$ and $E_V$ at Strouhal numbers $S_{tr} = 0.039, 0.060$.

Fig. 9 shows the contour lines of the dimensionless power density spectra $E_{\tilde{U}}, E_{\tilde{V}}$ of the coherent velocities. On the top, the contours for the primary instability at $S_{tr} = 0.656$ and the first sub-harmonic are shown. This value is of the same magnitude as the Strouhal number of 0.726 reported by Sakakibara et al. (1978) in a plane free jet at $Re = 10{,}300$. The secondary instability and its first sub-harmonic are shown at the bottom.
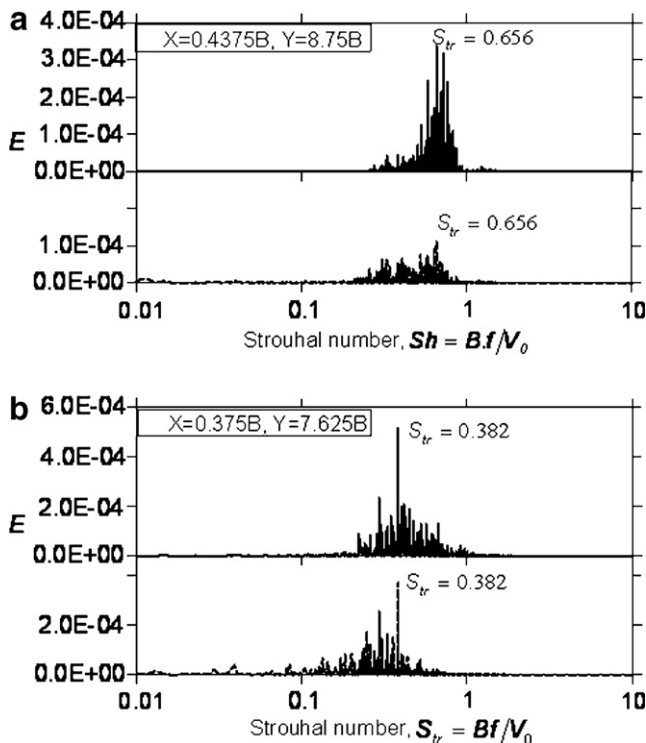


Fig. 11. Power density spectra of velocity fluctuations $u$ and $v$ at $(x/B, y/B) = (0.4375, 8.75)$ and $(0.375, 7.625)$.

The contour lines clearly reveal that the high frequency components associated with the smaller eddies are found near the nozzle, as they should, while the sub-harmonic components associated with the larger eddies are located further downstream. It is clear also that the transverse velocity spectrum appears better defined than the streamwise velocity spectrum.

Fig. 10 provides the same information about the larger size, lower frequency structures located for the most part near the wall. It can be noticed from the picture that the isocontours of $E_{\tilde{V}}$ are smoother and better defined in this case than they were for the higher frequencies. The complete power density spectra $E_u$ and $E_v$ for the velocity fluctuations $u$ and $v$ at the two positions shown in Fig. 8 are presented in Fig. 11. The spectra are continuous, as they are expected to for a random fluctuation, with vanishing energy at very high and very low frequencies. They display however a peak of energy density at $S_{tr} = 0.656$ for position a, which is closer to the nozzle, and at $S_{tr} = 0.382$ for position b, which is more remote. The spectrum of the pressure fluctuations at the stagnation point, shown
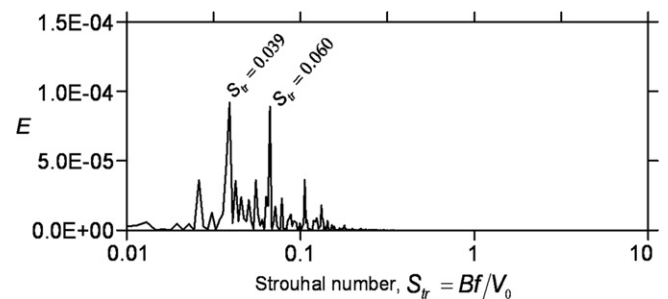


Fig. 12. Power density spectra of pressure fluctuation at stagnation point.

in Fig. 12, also involve energy peaks at $S_{tr} = 0.039$ and 0.060, for which the isocontours were presented in Fig. 10.

## 5. Conclusion

It appears that the unsteady averaging approach of Ha Minh, when used in conjunction with the eddy-viscosity model of Myong and Kasagi, is able to reproduce, from steady boundary conditions, the two-dimensional structures of pseudo-periodic character found experimentally in the impinging jet at the Reynolds number considered. Despite the inherent limitations of the Boussinesq closure, near the stagnation point or in the wall jet region for instance, the presence of the coherent parts of the mean quantities in the numerical solution will improve to some extent the predictions of the time-averaged Reynolds stress components. Spectral analysis also reveals that the coherent part of the solution obtained here is compatible with the coalescence of the eddies originating from the instabilities in the shear layer near the nozzle and sub-harmonic generation.

## Acknowledgements

## Appendix

In fully-developed pipe flow for instance, the turbulent transport equations in cylindrical coordinates reduce using Eqs. (9), (10) to:

$$0 = \frac{1}{r}\frac{d}{dr}\left(r\,v_k\frac{dk}{dr}\right) + v_T\left(\frac{d\overline{U}}{dr}\right)^2 - \varepsilon$$

$$0 = \frac{1}{r}\frac{d}{dr}\left(r\,v_\varepsilon\frac{d\varepsilon}{dr}\right) + C_{1\varepsilon}C_\mu f_\mu k\left(\frac{d\overline{U}}{dr}\right)^2 - C_{2\varepsilon}f_{2\varepsilon}\frac{\varepsilon^2}{k}$$

(A.1)

For a pipe radius $a$, the distance from the wall is simply $y = a - r$. The scaling

$$y^+ = \frac{u_* y}{v}, \quad \overline{U}^+ = \frac{\overline{U}}{u_*}, \quad \xi = \frac{v}{u_* a}$$

(A.2)

yields the convenient formulas :

$$\frac{d}{dr} = -\frac{u_*^2}{v}\frac{d}{dy^+}$$

$$\frac{1}{r} = \frac{\xi}{1 - \xi y^+}\frac{u_*}{v}$$

(A.3)

In terms of the dimensionless quantities $k^+ = k/u_*^2$ and $\varepsilon^+ = v\varepsilon/u_*^4$, Eq. (A.1) becomes:

$$0 = \frac{d}{dy^+}\left(\frac{v_k}{v}\frac{dk^+}{dy^+}\right) - \frac{\xi}{1 - \xi y^+}\frac{v_k}{v}\frac{dk^+}{dy^+} + \frac{v_T}{v}\left(\frac{d\overline{U}^+}{dy^+}\right)^2 - \varepsilon^+$$

$$0 = \frac{d}{dy^+}\left(\frac{v_\varepsilon}{v}\frac{d\varepsilon^+}{dy^+}\right) - \frac{\xi}{1 - \xi y^+}\frac{v_\varepsilon}{v}\frac{d\varepsilon^+}{dy^+}$$

$$+ C_{1\varepsilon}C_\mu f_\mu k\left(\frac{d\overline{U}^+}{dy^+}\right)^2 - C_{2\varepsilon}f_{2\varepsilon}\frac{\varepsilon^{+2}}{k^+}$$

(A.4)

We assume a power expansion in $\xi$ for all variables, of the form :

$$\overline{U}^+ = u_0(y^+) + \mathcal{O}(\xi)$$

$$k^+ = k_0(y^+) + \mathcal{O}(\xi)$$

$$\varepsilon^+ = e_0(y^+) + \mathcal{O}(\xi)$$

$$\frac{v_T}{v} = n_0(y^+) + \mathcal{O}(\xi)$$

(A.5)

For sufficiently large $y^+$, $u_0 = 1/\kappa \ln(y^+) + C$ and $n_0 = \kappa y^+$, where $\kappa$ is the Von Kármán constant. This result is independent of the turbulence model used. Considering that $v \ll v_T$ and $1 \ll n_0$ when $y^+ \gg 1$, it follows that to the leading order $v_k/v = n_0/\sigma_k$, $v_\varepsilon/v = n_0/\sigma_\varepsilon$ and $R_T = k_0^2/e_0$. Setting the damping functions equal to one in the logarithmic zone, we can also deduce from Eqs. (4), (A.4), and (A.5) that:

$$\frac{d}{dy^+}\left\{\frac{n_0}{\sigma_k}\frac{dk_0}{dy^+}\right\} + n_0\left(\frac{du_0}{dy^+}\right)^2 - e_0 = 0$$

$$\frac{d}{dy^+}\left\{\frac{n_0}{\sigma_\varepsilon}\frac{de_0}{dy^+}\right\} + C_{1\varepsilon}C_\mu k_0\left(\frac{du_0}{dy^+}\right)^2 - C_{2\varepsilon}\frac{e_0^2}{k_0} = 0$$

(A.6)

$$n_0 = C_\mu\frac{k_0^2}{e_0}$$

Let us mention that the same derivation leads to identical equations in the case of a plane channel and also for a boundary layer. The wall region is not influenced therefore by curvature at the leading order in $\xi$. The first equality in Eq. (A.6) may be written as follows:

$$n_0\frac{d}{dy^+}\left\{\frac{n_0}{\sigma_k}\frac{dk_0}{dy^+}\right\} + \frac{n_0^2}{(\kappa y^+)^2} - n_0 e_0 = 0$$

$$\Rightarrow n_0\frac{d}{dy^+}\left\{\frac{n_0}{\sigma_k}\frac{dk_0}{dy^+}\right\} + 1 - C_\mu k_0^2 = 0$$

(A.7)

Thus, $k_0 = 1/C_\mu^{1/2}$ is a solution of Eq. (A.7). The equality $n_0 = \kappa y^+ = C_\mu k_0^2/e_0$ immediately implies that $e_0 = 1/\kappa y^+$. The corresponding turbulent Reynolds number is then $R_T = \kappa y^+/C_\mu$. The dimensional counterparts of $k_0$ and $e_0$ form the standard laws of the wall for $k$ and $\varepsilon$. Substituting $k_0$ and $e_0$ into the second equality of Eq. (A.6) yields after simplification $\kappa^2 = \sigma_\varepsilon C_\mu^{1/2}(C_{\varepsilon 2} - C_{\varepsilon 1})$ for the predicted value of the von Kármán constant, which is equal to $\kappa = 0.395$ in the present case.

# References

Anderson, S.T., Longmire, E.K., 1995. Particle motion in the stagnation zone of an impinging air jet. J. Fluid Mech. 299, 333–366.

Angioletti, M., Di Tommaso, R.M., Nino, E., Ruocco, G., 2003. Simultaneous visualization of flow field and evaluation of local heat transfer by transitional impinging jets. Int. J. Heat Mass Trans. 46, 1703–1713.

Aydore, S., Dissimile, P.J., 1997. Natural coherent structure dynamics in near field of fully turbulent axisymmetric jet. AIAA J. 35, 1171–1178.

Bradshaw, P., 1973. Effects of streamline curvature on turbulent flow. AGARDograph, no. 163.

Briley, W.R., 1974. Numerical method for predicting three dimensional flows in ducts. J. Comp. Phys. 14, 8–28.

Craft, T.J., 1991. Second-moment modelling of turbulent scalar transport. Ph.D. thesis, UMIST, Manchester.

Craft, T.J., Launder, B.E., Suga, K., 1997. Prediction of turbulent transitional phenomena with a nonlinear eddy-viscosity model. Int. J. Heat Fluid Flow 18, 15–28.

Ghia, U., Ghia, K.N., Shin, C.T., 1982. High-Re solutions for incompressible flow using the Navier–Stokes equations and a multigrid method. J. Comp. Phys. 48, 387–411.

Gresho, P.M., Sani, R.L., 1987. On pressure boundary conditions for the incompressible Navier–Stokes equations. Int. J. Numer. Meth. Fluids 7, 1111–1145.

Gutmark, E., Ho, C.-M., 1983. Preferred modes and the spreading of jets. Phys. Fluids 26 (10), 2932–2938.

Ha Minh, H., 1994. Order and disorder in turbulent flows: their impact on turbulence modelling. Osborne Reynolds Centenary Symp., UMIST, Manchester.

Ha Minh, H., Kourta, A, 1993. Semi-deterministic turbulence modelling for flows dominated by strong organized structures. In: 9th Symp. Turb. Shear Flows, Kyoto, Japan, 8–10 September.

Hanjalić, K., Launder, B.E., 1976. Contribution towards a Reynolds-stress closure for low-Reynolds-number turbulence. J. Fluid Mech. 74 (Pt. 4), 593–610.

Ho, C.M., 1982. Local and global dynamics of free shear layers. In: Proc. Symp. on Numerical and Physical Aspects of Aerodynamics Flows. Springer, pp. 521–533.

Hsiao, F.B., Huang, J.M., 1990. On the evolution of instabilities in the near field of a plane jet. Phys. Fluids A2, 3, 400–412.

Hussain, A.K.M.F., Reynolds, W.C., 1970. The mechanics of an organized wave in turbulent shear flow. J. Fluid Mech. 41 (Pt. 2), 241–258.

Lam, C.K.G., Bremhorst, K.A., 1981. Modified form of the $k$–$\varepsilon$ model for predicting wall turbulence. ASME J. Fluids Eng. 103, 4456–4460.

Launder, B.E., Sharma, B.I., 1974. Application of the energy dissipation model of turbulence to the calculation of flow near a spinning disk. Letters Heat Mass Trans. 1 (2), 131–138.

Mansour, N.M., Kim, J., Moin, P., 1988. Reynolds stress and dissipation rate budget in turbulent channel flow. J. Fluid Mech. 194, 15–44.

Myong, H.K., Kasagi, N., 1990. A new approach to the improvement of $k$–$\varepsilon$ turbulence model for wall-bounded shear flows. JSME Int. J., Series II 33 (1), 63–72.

Patel, V.C., Rodi, W., Scheuerer, G., 1985. Turbulence models for near-wall and low Reynolds number flows: a review. AIAA J. 23 (19), 1308–1319.

Pierrehumbert, R.T., Widnall, S.E., 1982. The two- and three-dimensional instabilities of a spatially periodic shear layer. J. Fluid Mech. 114, 59–82.

Reynolds, W.C., Hussain, A.K.M.F., 1972. The mechanics of an organized wave in turbulent shear flow. Part 3. Theoretical models and comparison with experiments. J. Fluid Mech. 54 (Pt. 2), 263–288.

Sakakibara, J., Hishida, K., Phillips, W.C.R., 1978. On the vortical structure in a plane impinging jet. J. Fluid Mech. 88 (Pt.4), 737–756.

Tsubokura, M., Kobayashi T., Taniguchi, N., 1997. Large eddy simulation of plane impinging jets. In: 11th Symp. Turb. Shear Flows, Grenoble, France, 8–10 September.

Tsubokura, M., Kobayashi, T., Taniguchi, N., Jones, W.P., 2003. A numerical study on the eddy structures of impinging jets excited at the inlet. Int. J. Heat Fluid Flow 24, 500–511.